**Geometrical matching in remote in-tube shock compression by an unsteady jet**

**D. Ichihara, D. Kuwabara, D. Moriyama, Y. Nakamura, A. Iwakawa, and A. Sasoh**

**Abstract**

Based on the Riemann problem in compressible fluid dynamics, if the head of an unsteady jet acts as a physical piston for air compression, a higher-pressure field than that of the kinetic pressure from a steady jet can be generated. In this study, the pressure characteristics of this air compression method, referred to as "remote in-tube air compression," were evaluated. The generated unsteady jet exhibited a high-pressure region in its central part that effectively acted as a physical piston (piston effect). Depending on the distance between the unsteady jet generator and a cylindrical test section, the overpressure inside the test section reached the maximum value when the cross-section of the jet head and the test section were matched. This matching condition was consistent with the in-tube pressure characteristics, thereby yielding an effective method for the remote generation of a high-pressure region using a simple device.

**Keywords:** Unsteady jet, Geometrical matching, In-tube compression, Riemann problem

**List of symbols**

| | |
|---|---|
| $D_{jet}$ | effective jet-head diameter |
| $D_n$ | nozzle inner diameter |
| $D_t$ | test-section inner diameter |
| $F_{jet}$ | compressing force of the unsteady jet |
| $\bar{I}_{eff}$ | effective momentum flux inside the test section |
| $\bar{I}_{jet}$ | momentum flux from jet |
| $\bar{I}_{leak}$ | momentum flux of the leakage flow |
| $L$ | distance between unsteady jet generator and test section |
| $L_{max}$ | distance at maximum $\Delta p_{T1,peak}$ |
| $L_{SW}$ | shock formation distance |
| $\Delta p$ | overpressure, pressure increment from the atmospheric condition |
| $p_1$ | initial absolute pressure |
| $p_2$ | absolute pressure behind a shock wave |
| $p_h$ | absolute pressure inside the high-pressure reservoir |
| $\Delta p_{T1,peak}$ | first peak overpressure at PT1 |

D. Ichihara (✉) · D. Moriyama · Y. Nakamura ·A. Sasoh
Department of Aerospace Engineering, Nagoya University, Furo-cho, Chikusa-ku, Nagoya 464-8603, Japan
e-mail: daisuke.ichihara@mae.nagoya-u.ac.jp
ORCID: 0000-0002-4249-9300
D. Kuwabara
Currently, NIPPON STEEL CORPORATION
6-1, Marunouchi 2-chome, Chiyoda-ku, Tokyo 100-8071, Japan
A. Iwakawa
Currently, Pale Blue Inc.
5-4-6 Kashiwanoha, Kashiwa-shi Chiba 277-0882 Japan

| | |
|---|---|
| $r$, $z$ | cylindrical coordinates |
| $t$ | time |
| $u$ | flow velocity inside the test section |
| $u_{\mathrm{p}}$ | piston velocity |
| $u_{\mathrm{jet}}$ | jet velocity |
| $u_{\mathrm{jet}}$ | leakage flow velocity |
| $z_{\mathrm{match}}$ | geometrical matching position |
| $\Delta z_{\mathrm{p}}$ | piston moving distance |
| $\xi$ | cross-section ratio |
| $\rho$ | mass density inside the test section |
| $\rho_{\mathrm{jet}}$ | mass density of jet |
| $\rho_{\mathrm{leak}}$ | mass density of leakage flow |
| $\tau_{\mathrm{eff}}$ | time duration for pressure rise at PT1 |
| $\tau_{\mathrm{open}}$ | time duration of piston motion |

## 1. Introduction

When a physical piston compresses in-tube static air, compression waves are generated, and the in-tube pressure increases. The compression waves are transformed into a shock wave after propagation over “shock formation” distances. In this case, the shock Mach number is dependent on the velocity field induced by the physical piston. Based on the same mechanism, a high-speed train generates compression waves that transform into shock waves ahead of the train, particularly in long tunnels [1]. When the shock wave is emitted at the tunnel exit, an impulsive sound referred to as a “tunnel sonic boom” is generated [2]. The train has a smaller effective cross-section than the tunnel, and this smaller cross-section results in a lower shock Mach number and overpressure behind the shock wave [3].

Moreover, an air-jet can generate an unsteady compression wave inside an open-end tube because the front of the jet acts as a physical piston, in a manner similar to the train. Kuwabara et al. demonstrated a significant pressure gain by emitting an air-jet apart from an unsteady jet generator that was set coaxially with respect to a cylindrical open-end tube [4]. This phenomenon is referred to as the “piston effect,” because the front part of the emitted jet acts as a physical piston. Based on this mechanism, an unsteady high-pressure field is generated at some distance from the unsteady jet generator. This “remote in-tube compression” mechanism is important in unsteady compressible fluid dynamics and is highly applicable as a local unsteady high-pressure-field generator. The expected pressure gain in atmospheric air ($p_1$ = 101.3 × 10$^3$ Pa) at 300 K can be estimated from compressible fluid dynamics theories [5]. The dynamic pressure $p_2$ generated by a stationary jet with a flow velocity of 100 m/s is $p_2/p_1$ = 0.06. By contrast, an unsteady jet with the same flow velocity is expected to have a dynamic pressure of $p_2/p_1$ = 1.25 based on a solution of the Riemann problem [6]. Based on this estimate, the unsteady jet can generate a pressure gain that is higher than that of the stationary jet by a factor of greater than 20.

However, no previous studies have systematically evaluated the pressure characteristics of remote in-tube compression. Therefore, the present study evaluated the relationship between the unsteady jet generated from a circular high-pressure chamber and the unsteady pressure field inside an open-end circular test section that was set coaxially with respect to the jet generator. The results indicated that the geometrical cross-section matching between the unsteady jet head and the inner diameter of the test section plays a critical role in maximizing the unsteady in-tube pressure gain.

## 2. Experimental apparatus and methods

Figure 1(a) presents the experimental setup employed in this study. The test section was a circular tube with an inner diameter of $D_t$, thickness of 10 mm, and total length of 500 mm. In particular, the right end was closed using a flange (outer diameter: 180 mm; thickness: 15 mm), and the left end was open. An unsteady jet generator was placed toward the open end of the test section on the common axis; thus, the unsteady jet impinged against the quiescent air in the test section. The separation distance from the exit of the unsteady jet generator to the open end was designated by $L$. In the test section, five piezoelectric pressure transducers (rise time = 1 μs, range = 689.4 kPa, Model 113B27, PCB Piezotronics, Inc.) were flush-mounted at 100 mm (PT1), 200 mm (PT2), 300 mm (PT3), and 400 mm (PT4) from the open end on the side wall and on the end flange (PT5). The pressure sensitivity and measurement resolution were 7.25 mV/kPa and $7.0\times10^{-3}$ kPa, respectively. The sensitivity validation is described in Appendix. The figure shows the cylindrical coordinates ($z$, $r$), where $z$ and $r$ are the axial and radial coordinates, respectively, with their origin set at the center of the exit plane of the unsteady jet generator.

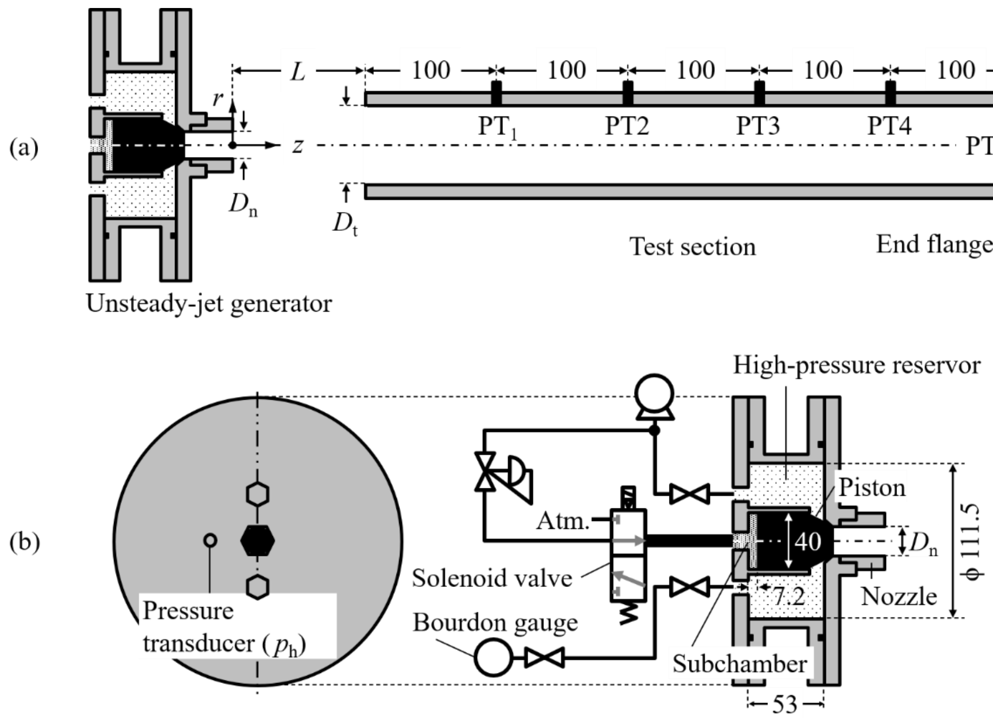


**Fig. 1 Schematic of experimental setup: (a) whole set up including the unsteady-jet generator and test section, (b) cross-section view of the unsteady-jet generator with air-driving circuit.**

Figure 1(b) presents a schematic of the unsteady jet generator. The generator contained a high-pressure air reservoir made of stainless steel (SUS304, ISO 4301-304-00-I), with an inner diameter of 111.5 mm and length of 53 mm. The time variation of the pressure in the reservoir $p_h$ was measured using a pressure transducer of the same type as that used in the test section. The sensor was flush-mounted on the end plate, and its radial position was 32 mm from the center axis. On the center axis, there was an open-ended cylinder with a diameter of 40 mm and length of 42 mm to guide the axial motion of the free piston. The outlet of the reservoir had a cylindrical nozzle with an inner diameter of $D_n$ (20 mm or 30 mm) and a length of 30 mm. Prior to a process cycle, the outlet was plugged by the free piston with a truncated cone head with an apex diameter of 20 mm and a full apex angle of 59°. The free piston, made of Monomer casting nylon, had a mass of 59

± 3.0×10$^{-4}$ g as measured by an electronic balance (AW320, Shimazu Corporation). The space behind the free piston acted as a subchamber in which the pressure was set independently from that in the high-pressure reservoir. For the experiment, the fill pressure was 700 kPa (absolute value). Two O-rings were set on the piston body to seal the gas in the sub-chamber while ensuring a smooth fit into the cylinder. The subchamber had an effective air slug length of 7.2 mm.

To inject an unsteady jet, the high-pressure air charged in the subchamber was released by opening the solenoid valve. Figure 2 presents the time history of the velocity $u_p$ and displacement $\Delta z_p$ of the piston motion that was calculated by the integration of $u_p$ with respect to time. The piston velocity was measured using a photonic Doppler velocimeter [7]. An oscilloscope (WavePro 7100, Teledyne Corporation) with a sampling rate of 20 GHz and bandwidth of 1 GHz was used for data logging. Under these conditions, the maximum measurable velocity was a 776 m/s with a resolution of 3.9 × 10$^{-2}$ m/s. During the release of the high-pressure air in the subchamber, $u_p$ gradually increased. When the piston arrived at the bottom end of the sub-chamber, $u_p$ had a maximum value of 6.7 m/s, and decreased abruptly to -2.4 m/s because the piston rebounded against the end wall. The time history of $u_p$ indicates that the piston opening time $\tau_{open}$ was 1.8 ms. Furthermore, Fig. 2 presents the absolute pressure variations in the high-pressure reservoir $p_h$. After the piston was completely opened, $p_h$ gradually decreased. When the piston was completely opened, $p_h$ decreased to 611 kPa, which was 87% of the initial condensation pressure. The Roman numbers in Fig. 2 represent the shutter timing of the shadowgraph images of the unsteady jet, as discussed in Section 3.2.

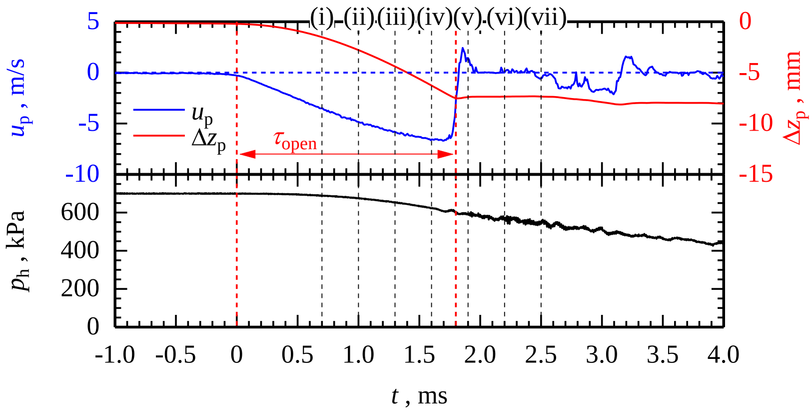


**Fig. 2 Time history of piston motion (velocity $u_p$ indicated by blue line, and displacement $\Delta z_p$ indicated by red line) and $p_h$.**

## 3. Results and discussion

### 3.1. Unsteady jet characteristics

First, the test section was removed, and the unsteady jet characteristics were evaluated. Figure 3 presents the shadowgraph images of an unsteady jet with $D_n$ = 20 mm (left) and 30 mm (right), respectively. The frame interval was 0.3 ms. Unlike an orifice-jet that has a constant diverging angle [8], the outer boundary (slip line) of the generated jet was rather parallel to its central axis for both values of $D_n$. However, as shown in frame (v), for $D_n$ = 20 mm, the slip line of the jet gradually expanded from the exit plane of the jet generator, whereas for $D_n$ = 30 mm, the jet had a smaller diameter than $D_n$ at the exit plane and this diameter gradually reduced. These differences are attributed to the under- and overexpansion of the jet, respectively. A one-dimensional, isentropic expansion flow-field was assumed between the high-pressure chamber and the nozzle. When the piston was completely opened, the minimum cross-section (throat area) comprised the piston, the inner wall of the high-pressure chamber was 316 mm$^2$, and $p_h$ was 611 kPa, as mentioned in Section 2. Based on these values and assumptions, the exit area for optimum expansion should be 468 $mm^2$ for correct expansion, which is equal to the area of a circular region with a diameter of 24 mm. Therefore, the nozzles with $D_n$ = 20 mm and 30 mm exhibited under- and overexpansion, respectively. In particular, for $D_n$ = 30 mm, the jet-head diameter was smaller than that of the nozzle, and the inner and the central parts of the jet oscillated at $z$ > 50 mm.

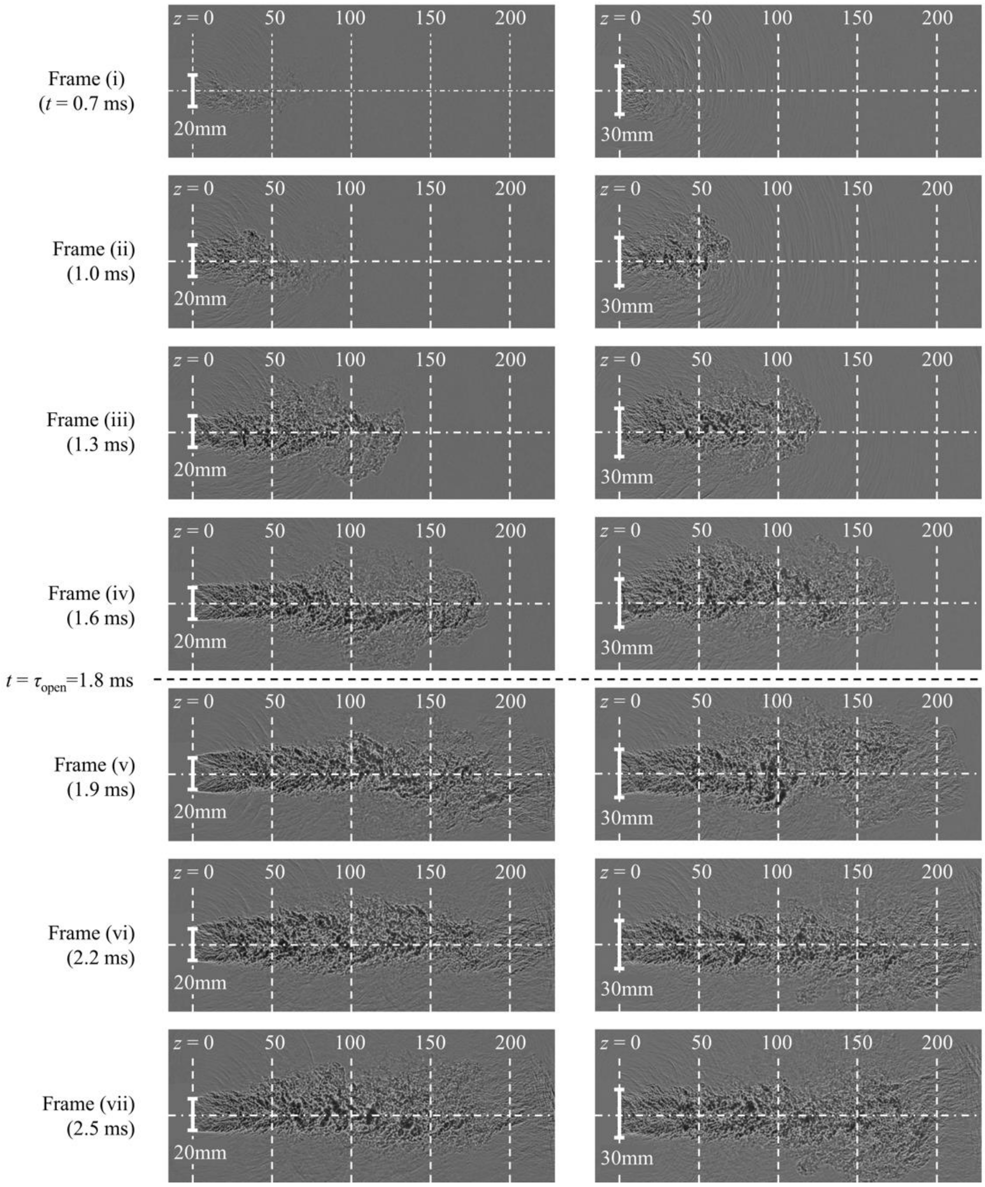


**Fig. 3 Shadowgraph images of unsteady jet (background noise was eliminated by subtracting a base image, captured before the event, from an original image): $D_n$ = 20 mm (left) and $D_n$ = 30 mm (right).**

Figure 4 presents the time histories of the Pitot pressure (overpressure) on the central axis $\Delta p(z,0)$, as obtained within the range of 50 mm ≤ $z$ ≤ 200 mm. The pressure sensor position was set by using JIS (Japanese Industrial Standard) first-class metal ruler with an uncertainty of ± 0.15 mm. The Roman numerals in Fig. 4 indicate each frame timing shown in Fig. 3. At each measurement point, the first overpressure peak, indicated by a black arrow, corresponds to the arrival of the jet front. Based on these timings, the propagation velocities were calculated by linear approximation as 164 ± 17 m/s (± 10%) for $D_n$ = 20 mm and 163 ± 23 m/s (± 14%) for $D_n$ = 30 mm, respectively.

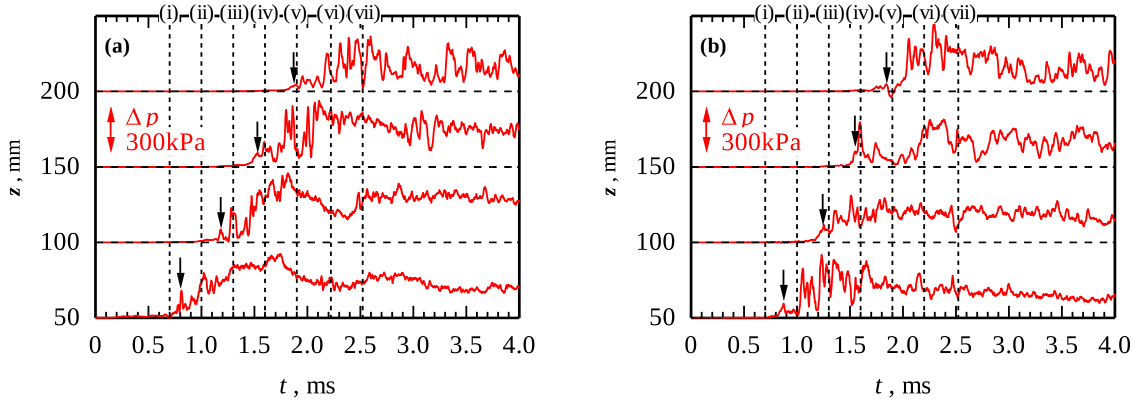


**Fig. 4 Time history of Pitot pressure (overpressure) on central axis: (a) $D_n$ = 20 mm and (b) $D_n$ = 30 mm.**

Figure 5(a) presents the spatial variations of the peak value of the Pitot pressure on the central axis, $\Delta p(z,0)$. To focus on the forefront pressure of the unsteady jet, the first peaks indicated by the black arrows in Figs. 4(a) and (b) were evaluated. The peak pressure were the same ($D_n$ = 20 mm) or slightly increased with increasing $z$ ($D_n$ = 30 mm) in the 50 mm ≤ $z$ ≤ 100 mm range and then decreased with increasing $z$ for $z$ ≥ 100 mm for both values of $D_n$. For $D_n$ = 20 mm, the peak overpressure abruptly decreased within the range of 150 mm < $z$ < 250 mm. For $z$ < 250 mm, smaller $D_n$ values corresponded to higher peak overpressures. In particular, at $z$ = 50 mm, the peak overpressures were 87 kPa and 95 kPa for $D_n$ = 20 mm and 30 mm, respectively, whereas at $z$ ≥ 250 mm, the peak overpressures for different $D_n$ values converged.

To estimate the effective diameter of the unsteady jet, the Pitot pressure was measured with respect to different radial positions up to $r$ = 50 mm, as shown in Fig. 5 (b). The measured overpressure at a radial position $r$ was normalized by the central value $\Delta p(z,0)$. For the nozzle with $D_n$ = 20 mm, a piston-like pressure distribution was observed at $z$ < 200 mm, and the high-pressure region was distributed within $r$ ≦ 10 mm, corresponding to $D_n$. For $z$ > 200 mm, the pressure gradient in the radial direction was gradually mitigated, and a uniform distribution was observed in the wider region. For $D_n$ = 30 mm, the high-pressure region was also within $r$ ≦ 10 mm. However, within the range of 50 mm < $z$ < 200 mm, the high-pressure region was expanded to $r$ = 20 mm.

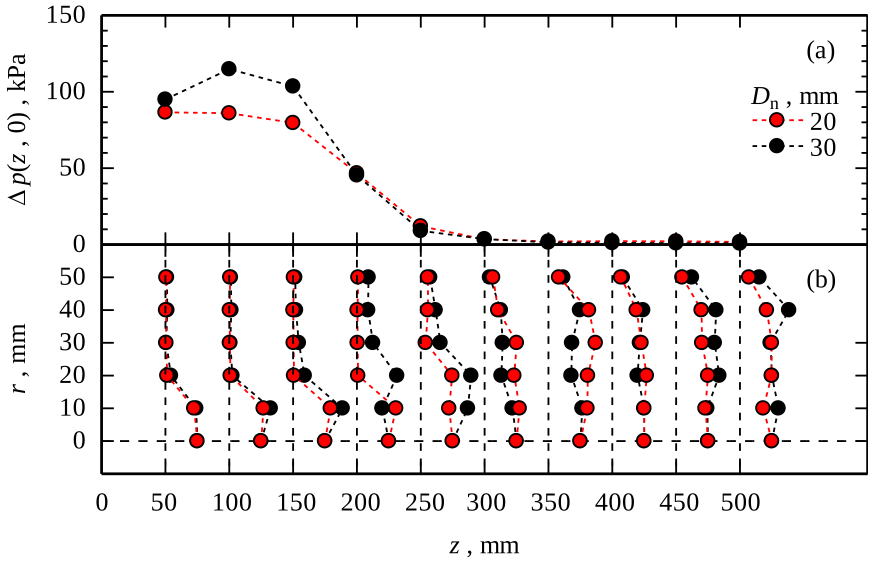


**Fig. 5 Spatial distributions of Pitot pressures (overpressure) with respect to different $D_n$ values: (a) $\Delta p(z,0)$ and (b) normalized Pitot pressure $\Delta p(z,r)/\Delta p(z,0)$.**

Based on the spatial distribution of the Pitot pressure (see Fig. 5 (b)) with linear interpolation, the effective diameter of the jet-head $D_{\text{jet}}$ and the compressing force $F_{\text{jet}}$ were calculated as follows:

$$\Delta p\left(z, D_{\text{jet}}/2\right) \equiv \max\left\{\Delta p\left(z,r\right)/2;\quad 0\text{mm} \le r \le 50\text{mm}\right\}. \tag{1}$$

$$F_{\text{jet}}\left(z\right) \equiv \int_{r=0\text{mm}}^{r=50\text{mm}} 2\pi r \Delta p\left(z,r\right) dr. \tag{2}$$

The values indicated by the black arrows in Figs. 4 (a) and (b) were used in Eqs. (1) and (2). The calculated $D_{\text{jet}}$ and $F_{\text{jet}}$ are shown in Fig. 6. Based on the law of propagation of errors, the relative uncertainties of $D_{\text{jet}}$ and $F_{\text{jet}}$ were less than 3.5% and 5.1%, respectively. At $z \le 100$ mm, $D_{\text{jet}}$ was not significantly dependent on $D_n$ due to the similar pressure distribution (see Fig. 5(b)). Within the 200 mm ≦ $z$ ≦ 350 mm range for $D_n$ = 20 mm case, $D_{\text{jet}}$ increased rapidly to 100 mm, and saturated at $z > 350$ mm. For $D_n$ = 30 mm case, $D_{\text{jet}}$ showed an apparent plateau in the 150 mm ≤ z ≤ 250 mm region because the pressure sensor head had a diameter of 5 mm and the spatial variation of the overpressure within this scale cannot be resolved. Moreover, $F_{\text{jet}}$ exhibited a similar dependence on $z$, regardless of $D_n$: for 50 mm ≤ $z$ ≤ 100 mm, $F_{\text{jet}}$ increased slightly and then decreased with increasing $z$. For 100 mm ≦ $z$ ≦ 300 mm, $F_{\text{jet}}$ decreased sharply. For $z > 300$ mm, $F_{\text{jet}}$ converged to 14 ± 2.7 N and 7.5 ± 0.9 N for $D_n$ = 20 mm and 30 mm, respectively.

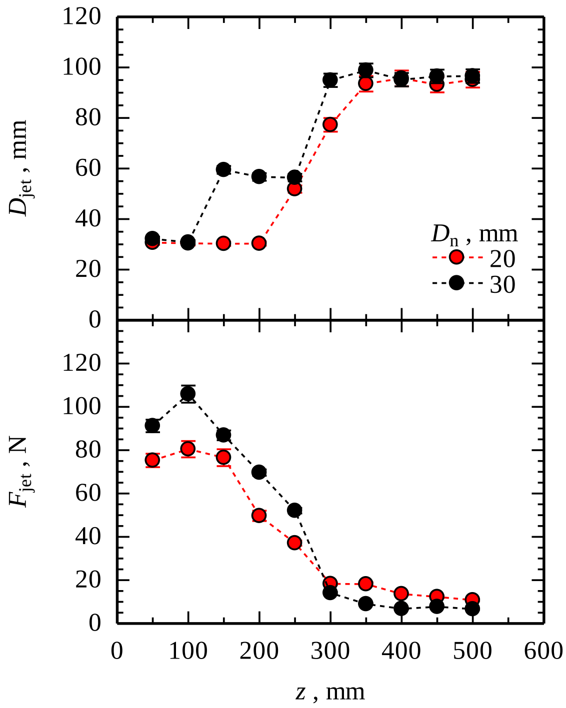


**Fig. 6 Spatial distribution of $D_{\text{jet}}$ and $F_{\text{jet}}$ with respect to different $D_n$ values.**

### 3.2. Characteristics of pressure profiles inside test section

Figure 7 presents an example of the overpressure time histories measured inside the test section for $D_n$ = 20 mm, $D_t$ = 30 mm, and $L$ = 200 mm. For each pressure history measured by the pressure transducers flush-mounted on the inner wall of the tube (from PT1–PT4), two pressure jumps were observed. The first jump indicated by the black arrow was due to the compression waves or a shock wave driven by the unsteady jet [4]. Prior to the first jump, the overpressure gradually increased because the jet formation was not fully developed during the opening period of the piston. In particular, the mass flow rate and momentum flux of the jet were small. The second jump corresponded to the shock wave reflected from the end wall of the test section. Based on the wave diagram tracing the first pressure peaks, the propagation velocity of the compression/shock wave was calculated as 480 m/s. In the test section, the durations of the first peak for PT1–PT4 were 224, 64, 58, and 20 μs, respectively, showing a gradual decrease. Here, we defined the initial rise time, indicated by the black point, as 10% of the first peak pressure. Therefore, the transition to a shock wave was observed. Through the extrapolation of the streamline of the jet-front and that of the fist peak to $z = L$ (test section inlet), the effective duration for the first overpressure jump at PT1, namely, $\tau_{eff}$, was estimated as 0.3 ms, which was 16% of $\tau_{open}$. Given that the propagation time from the test section inlet to the pressure sensor PT1 ($z = L + 100$ mm) at sonic speed was 0.3 ms, it was found that inside the test section, the jet-front propagated with the sonic speed and only the first part of the jet influenced the first overpressure jump.

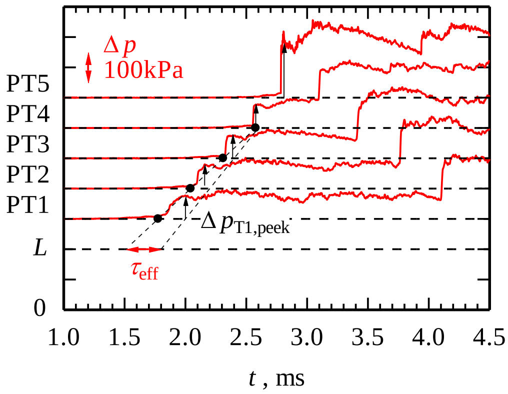


**Fig. 7 Time histories of pressure inside test section: $D_n$ = 20 mm, $D_t$ = 30 mm, and $L$ = 200 mm.**

Figures 8(a) and (b) present the variations of the first peak overpressure at PT1 (indicated by the arrow at PT1 in Fig. 7), namely, $\Delta p_{T1,peak}$, with respect to different values of $D_t$. Under each condition, five cycles were conducted. The symbols indicate that the average value and length of the error bars were two times the standard deviation (2σ). For $D_n$ = 20 mm (see Fig. 8(a)), $\Delta p_{T1,peak}$ had a maximum value within 150 mm < $L$ < 350 mm. The $L$ value for the maximum was dependent on $D_t$. For $D_t$ = 20–40 mm, the $\Delta p_{T1,peak}$ values were higher than those for $D_t$ = 60–90 mm. For $L$ = 200 mm, $\Delta p_{T1,peak}$ were 74, 72, 66, 38, 35, and 24 kPa for $D_t$ = 20, 30, 40, 60, 75, and 90 mm, respectively. For $L$ > 250 mm, $\Delta p_{T1,peak}$ decreased, and for $L$ = 500 mm, $\Delta p_{T1,peak}$ was lower than 20 kPa for all $D_t$ values. However, these pressure characteristics were not clearly observed for $D_n$ = 30 mm due to the jet oscillation [9] (see Fig. 3 right). For $D_t$ = 20 mm, $\Delta p_{T1,peak}$ was the highest for $L$ = 50 mm. Then, an overall monotonic decrease in $\Delta p_{T1,peak}$ with respect to $L$ was observed. For the other $D_t$ values, $\Delta p_{T1,peak}$ exhibited a maximum value within the 250 mm < $L$ < 300 mm range.

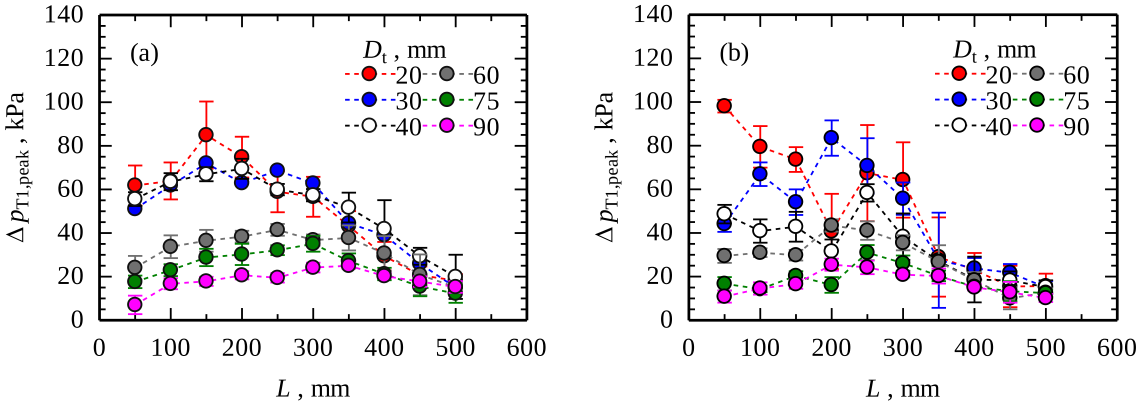


**Fig. 8 Peak pressure profile with respect to $D_t$: (a) $D_n$ = 20 mm and (b) $D_n$ = 30 mm.**

### 3.3. Matching between jet and tube projections

As shown in Fig. 8(a), $\Delta p_{\rm T1,peak}$ increased and exhibited a maximum value, and then decreased gradually with increasing $L$, particularly for $D_{\rm n}$ = 20 mm. The in-tube overpressure characteristics can be explained qualitatively based on the cross-section matching between the jet head and the test section. Figure 10(a) presents the spatial distribution of $(D_{\rm t}/D_{\rm jet})^2$ with respect to different $D_{\rm t}$ values for $D_{\rm n}$ = 20 mm. The relative uncertainty of $(D_{\rm t}/D_{\rm jet})^2$ was less than 7%. For $D_{\rm t}$ = 20 mm and 30 mm, the unsteady jet exhibited an almost equal or larger cross-section than that of the test section; namely, $(D_{\rm t}/D_{\rm jet})^2 \leq$ 1.0 for all $z$ values. From $D_{\rm t}$ = 40–90 mm, $(D_{\rm t}/D_{\rm jet})^2 >$ 1.0 at $z$ = 50 mm and decreased with increasing $z$. For $z$ = 500 mm, $(D_{\rm t}/D_{\rm jet})^2 \leq$ 1.0, regardless of $D_{\rm t}$. The axial position $z_{\rm match}$, where $D_{\rm jet} = D_{\rm t}$, was calculated by linear interpolation of the $(D_{\rm t}/D_{\rm jet})^2$ profile. Table 1 presents $z_{\rm match}$ with respect to different $D_{\rm t}$ values for $D_{\rm n}$ = 20 mm. The axial position $L_{\rm max}$, where $\Delta p_{\rm T1,peak}$ achieved the maximum value with respect to different $L$ values (see Fig. 8 (a)), was also summarized. Because $(D_{\rm t}/D_{\rm jet})^2 \leq$ 1.0 in all $z$ for $D_{\rm t}$ = 20 mm and 30 mm cases, $z_{\rm match}$ cannot be defined. For $D_{\rm t} \geq$ 40 mm cases, $L_{\rm max}$ values were similar to those of $z_{\rm match}$.

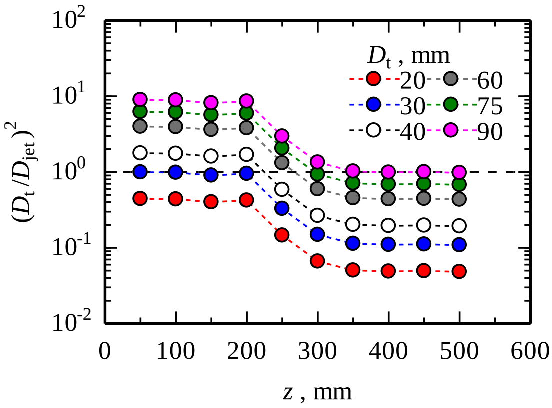


**Fig. 9 Spatial distribution of the cross-section ratio $(D_{\rm t}/D_{\rm jet})^2$ with respect to different $D_{\rm t}$ values for $D_{\rm n}$ = 20 mm.**

**Table 1 $L_{\rm max}$ and $z_{\rm match}$ with respect to different $D_{\rm t}$ values for $D_{\rm n}$ = 20 mm.**

| $D_{\rm t}$ mm | $z_{\rm match}$ mm | $L_{\rm max}$ Mm |
|---|---|---|
| 20 | - | 150 |
| 30 | - | 150 |
| 40 | 219 | 200 |
| 60 | 264 | 250 |
| 75 | 297 | 300 |
| 90 | 341 | 350 |

The in-tube overpressure depends on effective momentum flux $\bar{I}_{\rm eff}$ at PT1 defined as

$$\bar{I}_{\rm eff} \equiv \int_{r=0}^{r=D_{\rm t}/2} \rho(r) u^2(r)\cdot 2\pi r dr \Big/ \int_{r=0}^{r=D_{\rm t}/2} 2\pi r dr . \qquad (3)$$

The symbol where $\rho$ and $u$ are the mass density and flow velocity inside the test section, respectively. The upper bar means cross-sectional averaged value. The incident jet momentum can be described as

$$\bar{I}_{\rm jet} \equiv \int_{r=0}^{r=D_{\rm jet}/2} \rho_{\rm jet}(r) u_{\rm jet}^2(r)\cdot 2\pi r dr \Big/ \int_{r=0}^{r=D_{\rm jet}/2} 2\pi r dr . \qquad (4)$$

Here, $\rho_{\rm jet}$ and $u_{\rm jet}$ are the mass density and velocity of the jet head, respectively. A schematic illustration of $\bar{I}_{\rm eff}$ with different cross-section ratios $(D_t/D_{jet})^2$ is shown in Fig. 10. When $(D_t/D_{jet})^2 > 1.0$ (see Fig. 10 (a)), a central part of the test section ($r \le D_{jet}/2$) is compressed by the jet momentum and the momentum leakage $\bar{I}_{leak}$ appears around the jet boundary ($D_{jet}/2 < r \le D_t/2$) as described in Ref. 3. Therefore, $\bar{I}_{eff}$ can be described as

$$\begin{aligned}\bar{I}_{eff} &\equiv \int_{r=0}^{r=D_t/2} \rho(r)u^2(r)\cdot 2\pi r dr \Big/ \int_{r=0}^{r=D_t/2} 2\pi r dr \\ &= \left( \int_{r=0}^{r=D_{jet}/2} \rho_{jet}(r)u_{jet}^2(r)\cdot 2\pi r dr + \int_{r=D_{jet}/2}^{r=D_t/2} \rho_{leak}(r)u_{leak}^2(r)\cdot 2\pi r dr \right) \Big/ \int_{r=0}^{r=D_t/2} 2\pi r dr \\ &= \bar{I}_{jet}\left(D_{jet}/D_t\right)^2 + \int_{r=D_{jet}/2}^{r=D_t/2} \rho_{leak}(r)u_{leak}^2(r)\cdot 2\pi r dr \Big/ \int_{r=0}^{r=D_t/2} 2\pi r dr \end{aligned} \tag{5}$$

Here, $\rho_{leak}$ and $u_{leak}$ are mass density and velocity of the leakage flow, respectively. By defining $\bar{I}_{leak}$ as

$$\bar{I}_{leak} \equiv -\int_{r=D_{jet}/2}^{r=D_t/2} \rho_{leak}(r)u_{leak}^2(r)\cdot 2\pi r dr \Big/ \int_{r=D_{jet}/2}^{r=D_t/2} 2\pi r dr . \tag{6}$$

$\bar{I}_{eff}$ can be formulated as

$$\bar{I}_{eff} \equiv \bar{I}_{jet}\left(D_{jet}/D_t\right)^2 - \bar{I}_{leak}\left(1-\left(D_{jet}/D_t\right)^2\right). \tag{7}$$

When $(D_t/D_{jet})^2 = 1.0$ (see Fig. 10 (b)), the second term in Eq. (7) is zero and the jet momentum fully contributes to in-tube air compression, $\bar{I}_{jet} = \bar{I}_{eff}$. When $(D_t/D_{jet})^2 < 1.0$ (see Fig. 10 (c)), only a central part of the jet contributes to the air compression depending on the cross-section ratio. Therefore, the effective momentum flux should be $\bar{I}_{eff} = \bar{I}_{jet}(D_t/D_{jet})^2$. Therefore, the effective momentum flux inside the test section is maximum when $(D_t/D_{jet})^2 = 1.0$, namely for $D_{jet} = D_t$.

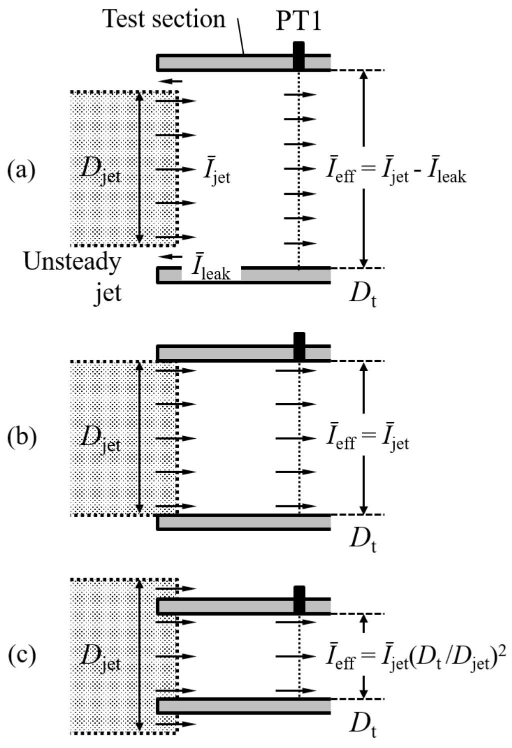


**Fig. 10 Schematic of the effective momentum flux $\bar{I}_{eff}$ inside the test section with different cross section ratios, (a) $(D_t/D_{jet})^2 > 1.0$, (b) $(D_t/D_{jet})^2 = 1.0$, and (c) $(D_t/D_{jet})^2 < 1.0$.**

### 3.4. Effective unsteady jet momentum for remote in-tube shock formation

Because $\bar{I}_{jet} \approx F_{jet}/(¼\pi D^2_{jet})$, for $(D_t/D_{jet})^2 \leq 1.0$ (see Fig. 10 (b) and (c)) $\bar{I}_{eff}$ can be represented as $\bar{I}_{eff} \approx F_{jet}\xi/(¼\pi D^2_t)$ with $\xi \equiv \min\{(D_t/D_{jet})^2, 1.0\}$. Figure 12 presents $F_{jet}\xi/(¼\pi D^2_t)$ with different $D_t$ values for $D_n$ = 20 mm case. For $z$ > 150 mm, $F_{jet}\xi/(¼\pi D^2_t)$ decreased rapidly which was consistent with the $\Delta p_{T1,peek}$ variation with respect to $L$ for $D_t$ = 20 mm and 30 mm cases (see Fig. 8 (a)). Assuming that the in-tube momentum from the unsteady jet is conserved, the incident local compression waves gradually merged and transformed to a normal shock wave so that the air inside the test section is compressed uniformly (see Fig. 7). At $L$ = 200 mm, where $D_{jet}$ = 30 mm, the shock formation distance $L_{SW}$ from the test section inlet was calculated from $L_{SW} = a_0 / (c - a_0)\ a_0\tau_{eff}$ [5]. Here, $a_0$ and $c$ are the speed of sound (= 343 m/s) and the characteristic velocity estimated from time history of pressure transducers (see Fig. 7). The calculated $L_{SW}$ is shown in Fig. 12. When $(D_t/D_{jet})^2 \leq 1.0$ ($D_t$ = 20 mm and 30 mm), $L_{SW}$ shows similar values of 335 mm and 353 mm for $D_t$ = 20 mm and 30 mm, respectively, because the effective compression pressure $F_{jet}\xi/(¼\pi D^2_t)$ is same (= 68.8 kPa, see Fig. 11). Whereas for $(D_t/D_{jet})^2 > 1.0$ ($D_t$ = 40, 60, 75, and 90 mm), $L_{SW}$ increased with increasing $(D_t/D_{jet})^2$ because $F_{jet}\xi/(¼\pi D^2_t)$ decreased. Therefore, remote in-tube compressible flow field and corresponding overpressure were successfully characterized by $(D_t/D_{jet})^2$ and $F_{jet}\xi/(¼\pi D^2_t)$.

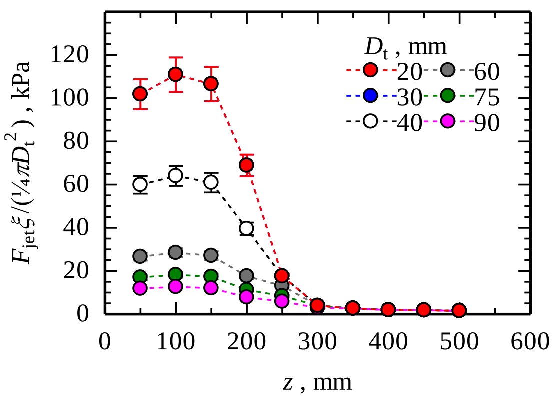


**Fig. 11 Special distribution of an effective compression pressure $F_{jet}\xi/(¼\pi D^2_t)$ for different $D_t$ values with $D_n$ = 20 mm.**

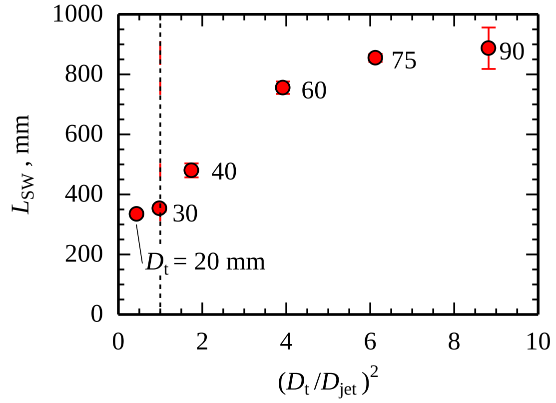


**Fig. 12 Shock formation distance from the test section inlet $L_{SW}$ with different $D_t$ values for $D_n$ = 20 mm, $L$ = 200 mm and $D_{jet}$ = 30 mm.**

## 4. Conclusions

In this study, a high-pressure field was remotely generated inside a cylindrical test section by using an unsteady jet with two different nozzle diameters. For both nozzle diameters, the jet exhibited a high-pressure region only in its central part, particularly within 200 mm from the nozzle exit plane. This high-pressure region acted as a physical piston (piston effect) and compressed the air in the test section. The effective jet-head diameter increased rapidly within the 200 mm < $z$ < 350 mm region. Due to this diameter expansion, the peak overpressure of the test section exhibited a maximum value with respect to the changes in the distance between the generator and the test section. When the cross-section of the jet and the test section were matched, the peak overpressure exhibited the maximum value. The cross-section of the test section was larger, and the distance required to satisfy the matching was longer. The presented matching characteristics successfully explain the in-tube pressure characteristics and provide an effective method for the remote generation of a high-pressure region.

**Acknowledgements**

This study was supported by Japan Society for the Promotion of Science (JSPS) KAKENHI grant no. 18H03813.

**Appendix**

The pressure sensitivity validation of piezoelectric pressure transducers (Model 113B27, PCB Piezotronics, Inc.) that were used in this study was conducted through a shock tube experiment. The details of shock tube apparatus have been described in our previous work [10]. The pressure sensors were located every 50 mm in the test section. When the driver and driven pressure were set to 93.3 kPa and 39.6 kPa, respectively, the shock Mach number was calculated as 1.18 by applying the time-of-flight method for pressure sensor signals. The measured overpressure behind the normal shock wave was 58.2 ± 0.013 kPa for five shot average. The theoretical overpressure estimated from the measured shock Mach number was 58.6 kPa, implying that the nominal pressure sensitivity is correct within a relative uncertainty of 0.7%. Thus, the pressure measurement is reliable with regard to both sensitivity and repeatability.

**References**

1 Miyachi, T.: Non-linear acoustic analysis of the pressure rise of the compression wave generated by a train entering a tunnel. J. Sound. Vib. 458, 365-375 (2019).
https://doi.org/10.1016/j.jsv.2019.06.033

2 Takayama, K., Sasoh, A., Onodera, O., Kaneko, R., Matsui, Y.: Experimental investigation on tunnel sonic boom. Shock Waves 5, 127-138 (1995).
https://doi.org/10.1007/BF01435520

3 Hara, T.: Aerodynamic force acting on a high speed train at tunnel entrance. Bulletin of JSME 4, 547-553 (1961).
https://doi.org/10.1299/jsme1958.4.547

4 Kuwabara, D., Kawasaki, H., Iwakawa, A., Sasoh, A., Yamashita, T., Taguchi, K.: In-tube shock wave compression by piston effect of unsteady jet. Bulletin of JSME 7, 19-00534 (2020).
https://doi.org/10.1299/mej.19-00534

5 Sasoh, A.: Compressible fluid dynamics and shock waves. Springer, Singapore (2020).
https://doi.org/10.1007/978-981-15-0504-1

6 Toro, E., F.: Riemann Solvers and Numerical Methods for Fluid Dynamics: a practical introduction. Springer, Singapore (2020).
https://doi.org/10.1007/b79761

7 Dolan, D. H.: Extreme measurements with photonic doppler velocimetry (PDV). Rev. Sci. Instrum. 91, 051501 (2020).
https://doi.org/10.1063/5.0004363

8 Volpe, J. A., Settles, G. S.: Laser-induced gas breakdown as a light source for schlieren and shadowgraph particle image velocimetry. Opt. Eng. 45, 080509 (2006).
https://doi.org/10.1117/1.2332867

9 Fei, L., Hejuan, C.: Numerical analysis of vortex shedding behavior of piezoelectric microgenerator from dynamic

airflow-induced vibration. Adv. Mat. Res. 694-697, 1595-1601 (2013).
https://doi.org/10.4028/www.scientific.net/AMR.694-697.1595
10 Tamba, T., Nguyen, T. M., Takeya, K., Harasaki, T., Iwakawa, A., Sasoh, A.: Counter-Driver Shock Tube. Shock Waves 25, 667-674 (2015).
https://doi.org/10.1007/s00193-015-0594-z